JATIS Journal of Astronomical Telescopes, Instruments, and Systems

RESEARCH PAPER

ORCAS Keck instrument demonstrator

Eliad Peretz,[a,*] Peter Wizinowich,[b] Maxwell A. Millar-Blanchaer,[c] Bert Pasquale,[a] Jason Chin,[b] Guillaume Filion,[d] Luke Gers,[b] Shui Hung Kwok,[b] Jean Thomas Landry,[d] Scott Lilley,[b] Eduardo Marin,[b] Sam Ragland,[b] Ed Wetherell,[b] Kevin Hall,[a] Jules Fowler,[e] Étienne Gauvin,[d] Rebecca Jensen-Clem,[e] Marc Kassis,[b] Peter Kurczynski,[a] John Mather,[a] Eric L. Nielsen,[f] John O'Meara,[b] Imke de Pater,[g] Peter Plavchan,[h] Steph Sallum,[i] Shobita Satyapal,[h] Brett Smith,[b] Kayla Carmical,[a] Jack Grossman,[c] Andrew Lewis,[a] Maya Wertheim,[a] and Vivian Palmer[a]

[a]NASA Goddard Space Flight Center, Greenbelt, Maryland, United States
[b]W. M. Keck Observatory, Kamuela, Hawaii, United States
[c]University of California Santa Barbara, Santa Barbara, California, United States
[d]OMP Inc., Quebec City, Quebec, Canada
[e]University of California, Santa Cruz, Santa Cruz, California, United States
[f]New Mexico State University, Las Cruces, New Mexico, United States
[g]University of California, Berkeley, Berkeley, California, United States
[h]George Mason University, Fairfax, Virginia, United States
[i]University of California Irvine, Irvine, California, United States

ABSTRACT. The Orbiting Configurable Artificial Star (ORCAS) mission in collaboration with the W. M. Keck Observatory has designed, assembled, built, and delivered, within 180 days, ORCAS Keck Instrument Demonstrator (ORKID) (ORCAS Keck Instrument Demonstrator), an early visible-wavelength performance demonstration with the Keck II Adaptive Optics (AO) system. The optical performance of ORKID meets the technical requirements derived from the scientific goals of having a Nyquist-sampled point spread function at 650 nm. This is achieved by diffraction-limited as-built performance with a root mean square internal wavefront error below 50 nm, which is key for the advancement of the ORCAS mission. ORKID has acquired, with a closed AO loop, no frame selection, while shifting and adding, the sharpest-ever on-sky image captured at Keck II. With a full width at half maximum of ~15 mas, this is the equivalent of a 9-m diffraction-limited telescope. By doing so, the immense potential and viability of the proposed Hybrid Observatory ORCAS mission are demonstrated.

Keywords: Orbiting Configurable Artificial Star; W. M. Keck Observatory; adaptive optics; artificial guide star; orbiting guide star; wavefront correction; visible instrument; hybrid observatories

Paper 24017G received Mar. 5, 2024; revised Feb. 17, 2025; accepted Mar. 11, 2025; published Mar. 28, 2025.

1 Introduction

The Orbiting Configurable Artificial Star (ORCAS) mission[1–5] is a first-of-its-kind hybrid space and ground observatory. It aims to complement and enable, at a SmallSat budget, new science accessible to future flagship-class missions over a decade from now (Fig. 1). This science would be enabled by the unprecedented angular resolution and sensitivity provided by ORCAS-enabled

*Address all correspondence to Eliad Peretz, eliad.peretz@nasa.gov

2329-4124/2025/$28.00 © 2025 SPIE

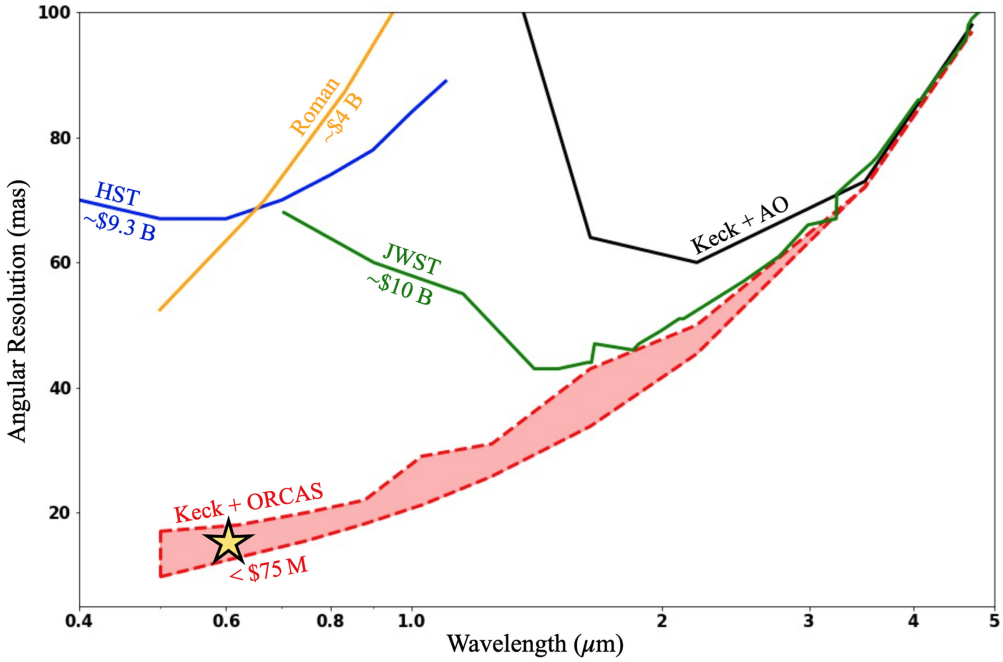

Fig. 1 Predicted angular resolution versus wavelength of selected future space missions/observatories. The region marked in red was predicted by the ORCAS mission as of 2020, the star indicates the ORKID system performance depicted in this paper. Predicted project budgets are provided for context. Notice that in principle a guidestar can be used by many other ground stations such as ELT/VLT/Subaru, for each one a different region of increased performance can be estimated. All data from previous and upcoming missions are drawn from their respective mission and/or instrument reports.

Adaptive Optics (AO)-corrected observations with large ground-based telescopes.[6] The ORCAS mission would provide a bright point source for AO wavefront sensing, tuneable across a large range of magnitudes (0th through 8th) and wavelengths (532, 778, 1064, and 1550 nm), allowing correction at visible and near-infrared (NIR) wavelengths with the W. M. Keck Observatory (WMKO) AO systems.[7,8] The low-cost ORCAS mission operating in collaboration with the WMKO would provide Great Observatory quality capabilities (in the league of major space telescopes) open to all US observers via a community-driven observation plan. These observations would result in unique science for the mission while also complementing and extending the science capabilities of Hubble Space Telescope (HST), James Webb Space Telescope (JWST), Roman, and other potential future missions.

Observations from space with Hubble, and now JWST, leverage their angular resolution and sensitivity abilities to perform major discoveries about our universe. These observatories rely on large ground observatories for follow-up observations. Telescopes such as the Keck Observatory rely on Adaptive Optics (AO) to partially correct the atmospheric turbulence that blurs their images. There are two primary methods to perform AO observations: (1) Natural Guide Stars (NGS) and (2) Laser Guide Stars (LGS). If a star of suitable brightness is within the vicinity of a desired science target, the observatory can lock on to it to perform corrections. NGS typically delivers the highest Strehl ratios, but the bright light from the guide star hinders the contrast. However, 99% of the sky is out of reach for NGS because there is a limited number of suitable stars. In the absence of a bright star near the chosen science target, the observer can create an artificial star by pointing a sodium (Na) laser, which excites the sodium layer. LGS observations suffer primarily from the Cone Effect, where the atmospheric turbulence affecting a star's wavefront is cylindrical, but the wavefront measured by the LGS is conical. As a result of that, among other reasons, only a partial correction can be performed.[8] The ORCAS mission can push the boundaries of ground-based AO observations by (1) providing a bright enough "artificial" NGS near any science target and (2) rejecting the bright laser from the ORCAS payload with a narrowband filter to maintain high contrast.

The ORCAS Keck Instrument Demonstrator (ORKID) project, a technology demonstrator for the ground segment, was developed to show the visible-wavelength performance potential of a bright source with the Keck II AO system, which is part of a three-stage technology development program effort which also includes AO imaging science targets with asteroids as moving guide stars and ultimately the usage of laser-carrying spacecraft operating in conjugation with Keck AO system. This demonstration (ORKID) has been successfully achieved with 15.2 mas full width at half maximum (FWHM) images at 650 nm. Two NSF-funded upgrades to the Keck II AO system are underway which will reduce the fitting error (replacing the current 349-actuator deformable mirror with a 2844-actuator deformable mirror) and bandwidth error (replacing the real-time computer with a machine capable of 1 ms control iterations[9]) of the current system, facilitating higher performance when using bright guide stars. Another ORKID demonstration underway is the use of moving asteroids for AO correction and implementing tracking wavefront sensors to keep a background target fixed on the science instrument, as well as post-processing of the data. These demonstrations will advance the ground system's operational and technological readiness level to the adequate level to propose the ORCAS mission. Ultimately, the ORCAS mission will provide the Keck II AO system with the capability to access "locked regions" of the night sky (i.e., regions of interest without access to nearby bright NGS) and near diffraction limited performance at a wide range of wavelengths.

In this paper, we establish the scientific and programmatic goals for ORKID in Sec. 2, formulate the instrument engineering requirements in Sec. 3, provide details of the optical and mechanical design of the instrument in Sec. 4, and conduct performance analysis in Sec. 5. Finally, we share preliminary on-sky results in Sec. 6 while leaving a detailed characterization of the visible-light AO performance and other instrument parameters for future work.

2 Scientific and Programmatic Goals

2.1 Science

Here, we highlight the primary science cases for ORKID, broken up into four main groups: solar system in Sec. 2.1.1, binary stars in Sec. 2.1.2, and accreting exoplanets in Sec. 2.1.3. For additional context, the full ORCAS mission science traceability matrix (STM) please see the ORCAS AS3 report.[6]

2.1.1 *Solar system science*

In the decades since the Voyager spacecraft flew past Neptune and Uranus,[10,11] the two planets have changed significantly. Uranus, initially devoid of significant cloud features, has revealed several large cloud features because the planet's north pole came into view.[12] Most intriguing are the polar cloud features, which have been detected in the H-band (1.63 μm), which can be discerned if the spatial resolution is high enough.[13] Neptune, on the other hand, has demonstrated a continuous evolution, with dark spots and huge storms (i.e., extremely bright clouds) infrequently appearing and disappearing.[14,15] Understanding the atmospheric dynamics that cause these features is a key step in understanding the detailed atmospheric structure of these planets, and progress can only be made through multi-wavelength (and hence multi-pressure-level) monitoring.

Ground-based observations in visible wavelengths would bring a wealth of additional information to ground-based NIR observations because different atmospheric depths are probed at different wavelengths. ORKID will enable monitoring of the two planets in and out of the methane band at wavelengths 889 and 643 nm, respectively. The contrast between clouds and background is highest at 889 nm, where we probe near the tropopause, whereas deeper layers are probed at 643 nm. This data can be compared with NIR images and extend wavelength (i.e., altitude) coverage of previous Keck data.

Titan's atmosphere consists primarily of N_2 gas with a few percent CH_4. Because Titan's surface temperature is close to the triple point of CH_4, this compound behaves such as water on Earth. A dense haze layer, produced via photolysis of CH_4, prevents probing the surface, except at a few wavelengths in the infrared (IR) and at 940 nm. ORKID will observe both at 889 and 940 nm to probe both the atmosphere and surface, respectively. It is expected that these

atmospheric and surface maps will produce the highest resolution features since Cassini, allowing us to search for changes in time.

Io is the most fascinating satellite; it is the most volcanically active body in our solar system and the only body with an SO_2-dominated atmosphere. Numerous volcanic eruptions have been detected at NIR wavelengths through hot spot (hot lava) emissions (e.g., Ref. 16). Several spacecraft missions have detected plumes associated with some hot spots, either directly and/or through changes in color on the satellite's surface. ORKID could potentially characterize changes on Io's surface as well as observe plumes directly.

Finally, due to the higher spatial resolution with Keck in the visible than the NIR, ORKID observations could include small bodies, such as asteroids and Kuiper Belt objects, which would allow for excellent shape determination and detection of moonlets and rings.

2.1.2 *Binary stars*

With the high spatial resolution afforded by ORKID in the visible spectrum, new stellar binaries can be imaged and the orbits of known binaries have the potential to be monitored with higher astrometric precision as compared with the IR. This could benefit a range of binary star science cases, including the dynamic measurement of stellar masses. Here, we motivate one impactful binary science case: the estimation of the ages of young moving groups.

To determine robust masses for imaged substellar companions, it is essential to have a well-defined age for the system. The host stars of most imaged planets to date reside in nearby young moving groups. A common method to determine the age of a young moving group is to use the Hertzsprung-Russel (HR) diagram position of the stars in the group combined with models of stellar evolution to find a best-fit age for all stars in the group. Measuring dynamical masses of moving group binary stars presents an opportunity to improve on this method, as they eliminate the degeneracy between mass, metallicity, and age in the color-magnitude diagram.[17] By combining resolved photometry and dynamical mass measurements, one can use a consistent framework to determine the age probability distribution of each component and, as a result, directly measure the age of the entire moving group.

Observations of binary stars with ORKID may provide better astrometric precision over NIR measurements because of the smaller point-spread function (PSF), improving the dynamical mass estimates. In addition, the new wavelength range will provide a critical lever arm on the stellar atmospheric models. To provide the best constraints on the stellar models, ORKID requires R, I, and z band measurements. To obtain the highest spatial resolution, ORKID requires fast-read modes for Lucky/Speckle Imaging at the shortest wavelengths and a non-redundant masking mode to push to the smallest angular separations.

2.1.3 *Accreting exoplanets*

Despite the thousands of known planets, scientific understanding of the early stages of planet formation is poorly constrained by observations. In particular, the details of mass delivery mechanisms and timescales at early ages are difficult to probe due to the paucity of accretion measurements. So far, accretion has been directly detected in only three cases, despite several searches:[18,19] the controversial LkCa 15b,[20–22] PDS 70 b and c,[23,24] and Delorme 1 (AB)b.[25] These initial detections allowed us to start constraining models,[26] but more measurements are needed. Leveraging Keck's NIR Pyramid wavefront sensor[27] and its 10-m aperture, the short wavelength coverage afforded by ORKID will enable new searches for H-alpha emission from accreting protoplanets around redder stars and at smaller inner working angles than previously accessible. These searches require the ORKID filter complement to include an H-alpha narrowband filter, as well as a continuum filter. When searching for accreting planets, ORKID will operate in a lucky imaging mode, a speckle imaging mode, and/or a non-redundant masking mode.

2.1.4 *Supermassive black holes and active galactic nuclei*

Current Keck NGS AO limits the number of accessible active galactic nuclei (AGN) targets due to their faintness and the extended nature of their core, making it hard or impossible for the AO system

to provide the high-order correction needed for visible-light imaging. Keck's current ground-based LGS system cannot provide good correction down to the visible regime. Nonetheless, we highlight here potential visible-light AGN science cases should an AO system (e.g., such as one that leverages ORCAS or a future visible-light AO system) be able to lock on these targets.

The discovery that at the heart of virtually all massive galaxies in the local Universe, lie supermassive black holes (SMBHs) strongly suggests that black holes play a pivotal role in the formation and evolution of galaxies. The well-known correlation between the black hole mass and the host galaxy's stellar velocity dispersion[28–31] launched a long-standing view that black hole growth and the build-up of galaxy bulges go hand-in-hand, perhaps as galaxy interactions fuel the central SMBH and grow the galaxy's bulge, and feedback from the AGN regulates the surrounding star formation in the host galaxy.[32–36] Although both simulations and theory support this general paradigm, the detailed physics surrounding the formation and growth of the black hole and its impact on the host galaxy are currently not well understood. Furthermore, binary SMBHs formed in galaxy mergers are one of the key contenders for the recently announced stochastic gravitational-wave background detected by pulsar timing arrays (ref). A clear understanding of the SMBH binary contribution to the gravitational wave (GW) background and future prospects for detecting SMBH binaries by the next generation of gravitational wave detectors requires a firm understanding of SMBH binary evolution, the pairing rate and distribution as a function of redshift, all of which are not well-constrained based on current observations. To make progress in the field, high spatial resolution observations across a significant portion of the sky are critical. ORKID and future-enabled spectroscopic instruments such as ORCAS will be a game changer in this field. High spatial resolution imaging in the optical enables the highest sensitivity and spatial resolution to probe the central parsecs in AGN hosts, within the gravitational sphere of influence of the black hole. Imaging observations alone can enable detailed morphological studies of AGN hosts down to spatial scales ($\approx$3 pc) corresponding to nuclear star clusters (NSCs) in a significant sample of galaxies for the first time. Such a study can establish the link between NSC properties and black hole properties. Imaging observations can also produce a sample of advanced mergers with closely separated galaxy nuclei down to 15 mas (corresponding to a few parsecs in the local universe and 100 pc at cosmic noon), an unprecedented regime of parameter space, providing some preliminary constraints on the rate and distribution of closely paired nuclei in the local Universe. Follow-up spectroscopy at high spatial resolution can identify accretion signatures, measure black hole masses, luminosities, and accretion rates; identify and measure outflows near their launch origin; and characterize the state and structure of the surrounding interstellar medium at unprecedented spatial resolution for the first time, allowing a first look into the detailed physics around accreting SMBHs in galaxy centers.

Models for their formation make divergent predictions for the mass distribution of intermediate-mass black holes, particularly in the range $10^2 - 10^4\,M_\odot$ at late times. ORCAS allows Keck to be uniquely suited to survey nearby dwarf galaxies and search for such black holes, which are the building blocks of both more massive galaxies and their SMBHs. These observations will resolve the cores of these systems to angular resolutions of $\sim$15 mas or better. Other ground-based [e.g., very large telescope/multi-conjugate-adaptive-optics-assisted visible imager and spectrograph (VLT/MAVIS)] and space-based (HST) facilities have insufficient resolution in optical wavebands to accomplish this science. Optical waveband observations are necessary to discriminate AGN from compact star clusters. A tractable goal is to find AGNs in dwarf galaxies by searching for broad lines. As a result, this survey will seek to determine the origins of SMBHs and solve one of the major unsolved mysteries in contemporary astrophysics.

Dual AGN is expected because galaxies grow and evolve via mergers and interactions, yet observations of dual AGN are exceedingly rare. Further observations could provide evidence of black hole growth through accretion, regulation of star formation, and that they are precursors of black hole mergers, which are strong emitters of gravitational radiation. In particular, probing close in mergers could shed light on difficulties with how theoretical models account for how SMBHs go from close encounters to candidates for a merger. To date, there is only one bound binary known[37] and only a handful with separations less than 3 kpc.[38–41] Current Keck AO can only resolve dual AGN to $\sim$50 pc resolution. At this distance, SMBHs are not yet gravitationally bound. However, diffraction-limited optical observations can probe this close-in region. These capabilities have been demonstrated in ORCAS asteroid studies (Hall et al. in prep).

AGN powers the flow of matter and energy from central engines to pervade their host galaxies. Outflows take the form of winds and jets; by studying them, we can better understand the role of AGN in regulating star formation in their host galaxies. Of critical importance is the capacity to spatially resolve the inner parsec scales of AGN to directly trace the gas. Currently, the best spatial resolution in the optical for nearby AGNs is ∼10 s of pc (Gemini Multi-Object Spectrograph-Integral Field Unit or Keck AO). ORCAS/Keck will probe the sub-kiloparsec scale to trace gas flows with prominent optical emission lines (e.g., OIII) and spatially resolved spectroscopy.

2.2 Programmatic Goals

One major goal of the ORKID effort is to demonstrate and characterize the performance of the current Keck II AO system at visible wavelengths, and in doing so retiring risk, raising technology readiness level (TRL), and informing the future design of ORCAS-WMKO mission instruments. Another goal is to foster successful collaboration between the ORCAS mission team and the WMKO team that allows for an observation plan guided by community engagement, providing high-performance AO to all U.S. astronomers. An additional timeline goal of less than 200 days was set, requiring the team to deliver the instrument, meeting the requirements, tight schedule, and budget.

Furthermore, we are interested in using ORKID to evaluate the current AO system's performance in the following ways:

1. Measuring the Strehl ratio and FWHM in short (10 ms) and long (several minutes) exposures over a range of wavelengths (595 to 970 nm) and guiding star magnitudes (0 to 10th).
2. Measuring the contrast ratio versus distance from the guide star.
3. Better understanding of the limitations of the current Keck AO system and what performance improvements are needed for impactful ORCAS science.
4. Determining how much tip-tilt performance improvement is needed to maintain close to diffraction-limited angular resolution. This can be seen in the evolution of image position between consecutive short-exposure images.
5. Using this experience as a step in developing a roadmap to visible science instrumentation to be developed for ORCAS.

Ultimately, the team was capable of designing, building, and commissioning the ORKID instrument, in under 200 days, to meet the requirements on both sides of the partnership and deliver results within the narrow time frame. However, the timeline drove several design and development decisions for ORKID. For instance, the opto-mechanical design choices minimized the number of parts needed, reducing fabrication time. Similarly, the optical module is capable of integrating two alternative stages due to shortages in the original chosen stage, and this allows for the instrument to be better adapted in the future. Ultimately, the strict 200-day timeline was chosen to ensure a full mission proposal by 2025. To this end, the team can quantify how fast development can move throughout the entire instrument design process. Furthermore, it provides an opportunity to identify the constraints imposed by the ground-based components during instrument development.

3 Instrument Requirements, Constraints, and Design Choices

The ORKID design is driven by the scientific and programmatic requirements presented in Sec. 2, which are derived from the ORCAS mission STM. In this section, technical requirements and constraints are presented. We list the opto-mechanical requirements for the science camera in Sec. 3.1 and discuss size and weight constraints with which the system needed to comply in Sec. 3.2.

3.1 Science Camera Opto-Mechanical Requirements

The following requirements were established for the science camera:

1. The visible science camera system shall be Nyquist sampled at 650 nm wavelength.
2. The plate scale shall be met within a tolerance of ±0.1 mas.

3. The visible science camera system shall provide a 10″ or larger unvignetted science field.
4. The transmitted wavefront quality through the visible camera system optics shall be less than 50 nm rms.
5. The throughput through the ORKID instrument shall be >90% between 595 and 970 nm wavelength.
6. A $2'' \times 2''$ science field shall be capable of being read out in 10 ms.
7. Differential atmospheric refraction (DAR) correction must be provided between the science and wavefront sensing wavelengths to maintain the science target position within 1/4 of the diffraction-limited image diameter over a 5-min observation sequence at a 45-deg zenith angle.
8. DAR over any 100 nm wavelength band between 600 and 1000 nm shall be less than 1/4 of the diffraction-limited image diameter at 45 deg zenith angle.
9. The visible science camera system shall provide a filter changer with at least six filter locations.
10. The filter changer shall be located as close as possible to the pupil plane to minimize field-dependent aberrations and to allow a pupil plane mask to be located in the filter wheel.
11. The visible science camera system shall be provided with a science-determined set of filters.
12. The visible camera system shall not vignette the 120″ diameter field to the AO acquisition camera.
13. The visible camera system shall be co-mounted on the same stage as the AO acquisition camera.
14. A beamsplitter shall be provided to split the 595 to 970 nm light between the visible science camera and the AO acquisition camera.

3.2 Footprint, Volume, and Weight Constraints

The physical location and size of a visible science camera were limited by the constraints of the Keck II AO bench. ORKID needed to be located in reflection from the dichroic beamsplitter that transmits light to the NIR science instruments. It could not interfere with the light to the existing visible wavefront sensors. Therefore, the visible science camera was integrated with the existing science camera with the existing acquisition camera (ACAM) as part of the ORKID package.

The ORKID assembly (A) and its location on the AO bench are shown in Fig. 2. The horizontal footprint of the existing ACAM system could not be exceeded to avoid interference with existing opto-mechanical systems. The vertical height was limited by the position of the optical axis above the AO bench (305 mm) and the height of the AO bench cover. The clearance of the delivered ORKID unit (vertical space between the unit and the AO bench cover) is 54 mm.

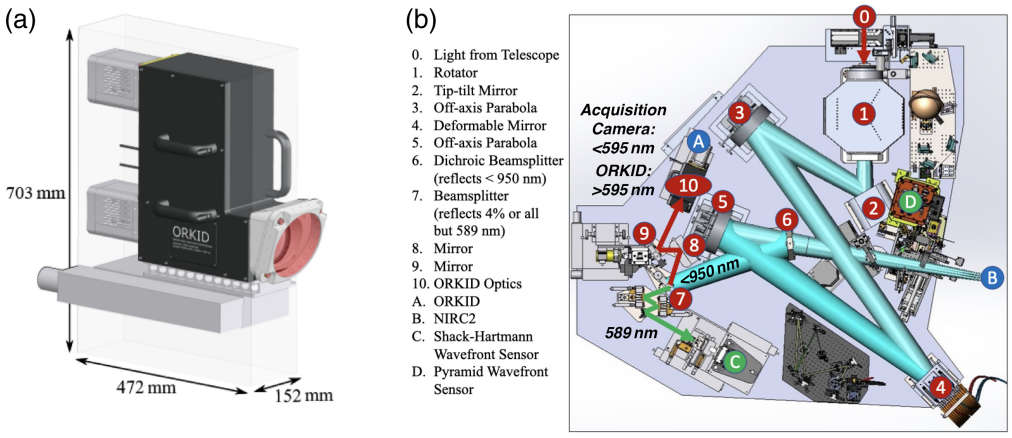

Fig. 2 ORKID system (a) and the envelope available to integrate the ORKID unit on the Keck II AO bench (b). In addition, we provide the full light path from the telescope to the ORKID instrument. The optional ACP can be seen on the left as a red plate attached to the ORKID system.

ACAM is mounted on a linear stage and pedestal, which were reused to support ORKID. The stage is used to focus ACAM on either a natural guide star (at infinity) or a laser guide star (as close as 85 km). If necessary, the handles shown in Fig. 2(a) can be removed to reduce the footprint.

An astigmatism corrector plate (ACP) can be mounted to the front of the ORKID assembly, as further described in Sec. 4.1.2. However, it is not currently required and extends outside the current ACAM envelope.

The maximum weight for the ORKID unit was set by the maximum allowed weight for the linear stage (90 kg); however, due to difficult installation access to the AO bench, the unit was designed to minimize weight.

4 Instrument Design

4.1 Optical Design

The ORKID optical system, shown in Fig. 3, includes the acquisition channel [120″ field-of-view (FOV)] and the science channel (10″ FOV). The driving science performance goal was Nyquist sampling (2 pixels) of a 650-nm diffraction-limited PSF. The main design constraint was the volumetric limits for being able to be placed on the very crowded Keck AO bench.

4.1.1 Optical layout

The ORKID instrument is placed at the focus of the AO bench visible light path at a plate scale of 0.727 mm/arcsecond. With a 100-mm acceptance aperture, this allows for the capture of the full 120-arcsecond diameter circular field that was passed through the AO rotator. A 250-mm focal length field lens converges the ray bundles to form a pupil at the acquisition camera lens. The 50 mm f/1.4 lens re-images the full-field telescope image onto the acquisition camera sensor.

Within the converging ray bundle following the field lens, a dichroic beamsplitter reflects the long wavelengths (>595 nm) to the science channel. A custom triplet lens captures the central 10-arcsecond field to re-image it at the science camera at f/34.3. At a camera plate scale of 6.7″/pixel, the 650-nm PSF FWHM covers two pixels.

Before reaching focus, the beam passes through several more optical elements. A pair of six-position filter wheels allow for bandpass filters and/or pupil masks to be placed into the beam. The first filter wheel is located at the pupil formed by the combination of the field lens and the triplet. It is there that either four filters or a pupil mask can be inserted into the beam. The pupil mask is used for non-redundant Aperture Masking Interferometry for increased angular resolution of a specific binary target. The second filter wheel contains five additional bandpass filters.

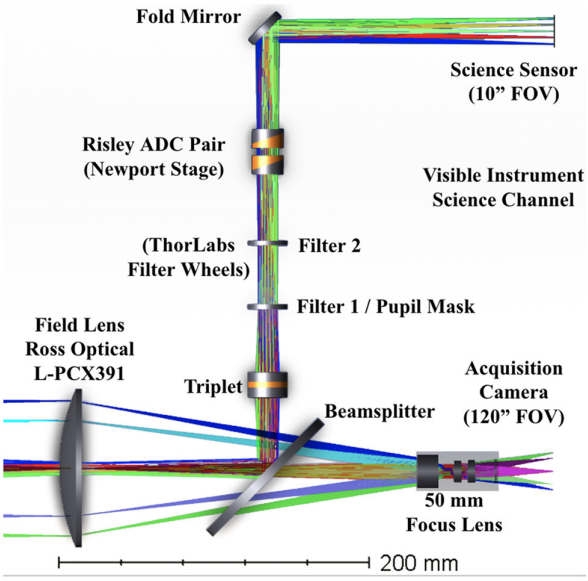

Fig. 3 Optical layout of the ORKID instrument.

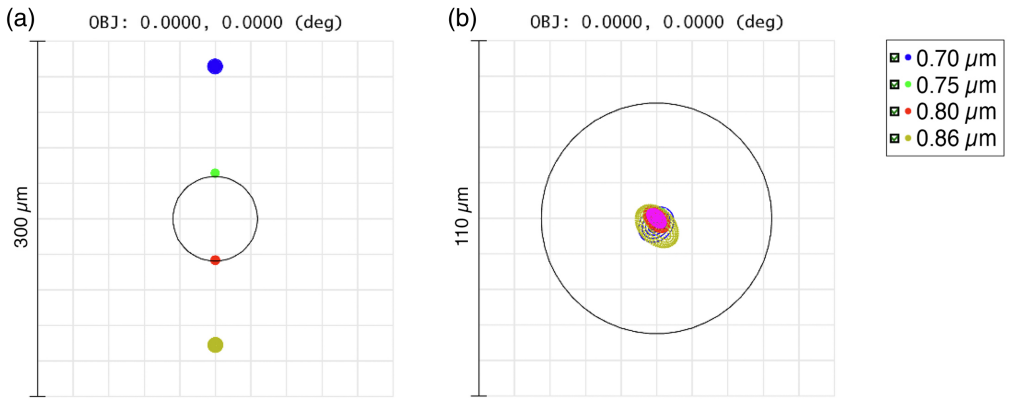

Fig. 4 Spectral correction with the ADC. (a) The full spectral range is shown at Zenith angle 45-deg (a) uncorrected and (b) when fully corrected for ORKID's viewable i Sloan bandpass (0.698 – 0.853 μm). The airy disc (black circle) for 700 nm is shown.

Either filter wheel can be used in the "open position," and the filters in the second wheel can be used in conjunction with the pupil mask of the first wheel. The second filter wheel is tilted by ~4 deg to avoid additional ghost reflections between the two filter wheels.

The next element in the optical train is the atmospheric dispersion corrector (ADC) Risley doublet prism pair mounted in dual rotation stages. At ORKID's magnification, when looking at an object 60 deg off zenith, the wideband image from 595 to 970 nm is dispersed into a spectrum more than 1.5-mm long due to the prismatic atmospheric dispersion. The ADC consists of a cemented pair of high-dispersion/low-dispersion glasses with matched indexes at ~650 nm to correct atmospheric dispersion. The two ADC prisms act in concert and can simultaneously counter-rotate to maintain the zenith dispersion direction and also rotate freely to match a desired pupil rotation. When counter-rotated at 0 deg, they cancel each other out and have no dispersive effect. When counter-rotated a full ± 90 deg, the prisms combine full efficacy to correct up to 60-deg Zenith dispersion up to the Sloan Z-band [830 to 1000 nm]. Their relative rotations are therefore adjusted as a function of waveband and Zenith. The resulting effect is shown in Fig. 4 for 45 deg Zenith when corrected for 700 to 860 nm (i Sloan bandpass). Note that for narrowband filters, dispersive correction is not needed, but they can still be used to keep an observed target centered on the sensor over various wavebands.

Finally, a single flat mirror is used to fold the optical path horizontally to the science camera sensor. The total optical path length allows the science camera and acquisition camera image planes to be vertically co-planar. This assures that the ORKID footprint did not increase from the original acquisition camera.

The total field distortion of the 10″ field is <0.2% or ± 0.001 mas/pixel. This is derived from the optical models of the telescope and camera. Within the central 2″, field distortion does not exceed 0.02%.

4.1.2 *Astigmatism correction*

The AO deformable mirror (Xinetics tweeter sampled 21×21 across the Keck pupil) can be used to remove astigmatism introduced by an IR-transmissive dichroic beamsplitter in the path to the IR science instruments. This action introduces astigmatism in the path to ORKID. To compensate for this, an ACP can be attached to the front of ORKID to apply the correction to the incoming beam, as shown in Fig. 5. The ACP is a 20-mm-thick fused silica plano-plano element. To accommodate different correction scenarios, various ACP plate holders can be attached or removed with a small adjustment in focus on the ORKID stage. The ACP is not currently mounted since simultaneous IR and visible science observations have not yet been performed.

4.1.3 *Stray light mitigation*

Stray light control keeps the image (signal) free of additional background noise that reduces the contrast and resolution of the camera output. To accomplish this, baffles are integrated on

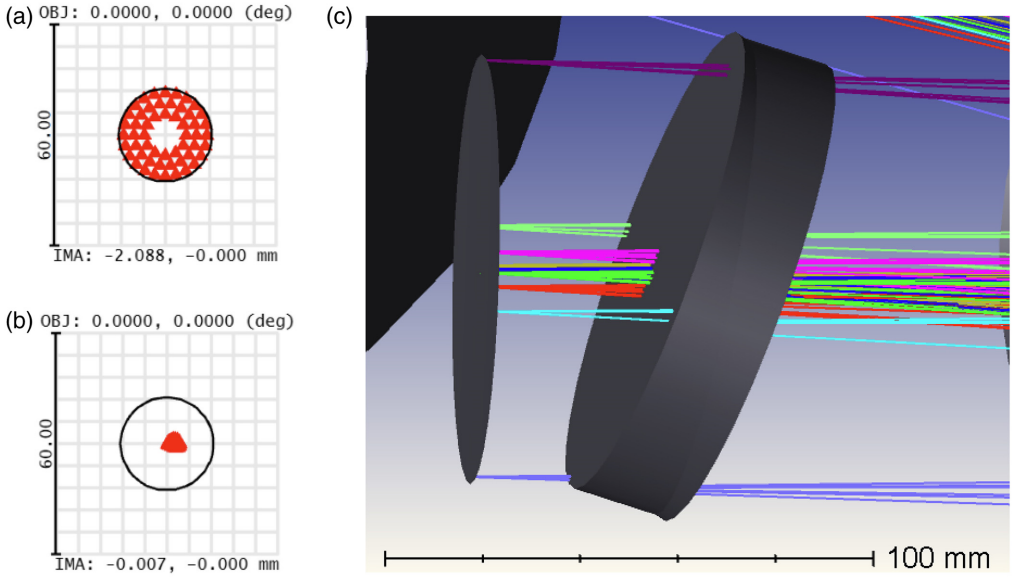

Fig. 5 Image correction by the use of the ACP. (a) Uncorrected spot. (b) Corrected spot. (c) ACP placement at ORKID entrance aperture.

element mounts (e.g., the triplet and ADCs) and other light paths to the sensors to prevent specular and "single bounce" scatter paths to the sensor. All non-bandpass refractive surfaces are anti-reflection-coated to minimize ghost reflections. Analysis shows any ghosts generated in the system have an extremely low (<0.1%) contribution to background noise.

4.2 Opto-Mechanical Design

The design of the opto-mechanical components of the ORKID instrument was done in a one-month schedule, which dictated many of the design choices. The instrument was thus designed to minimize the number of parts to reduce development and fabrication time. Figure 6 shows an isometric view of the computer aided design (CAD) model and the as-built instrument.

The main housing was designed out of a single piece of 6061-T6 aluminum to reduce the number of interfaces and ensure a stiff structure. The cover, also machined from a single piece of aluminum, is mounted on the main housing using captive fasteners. The instrument is mounted

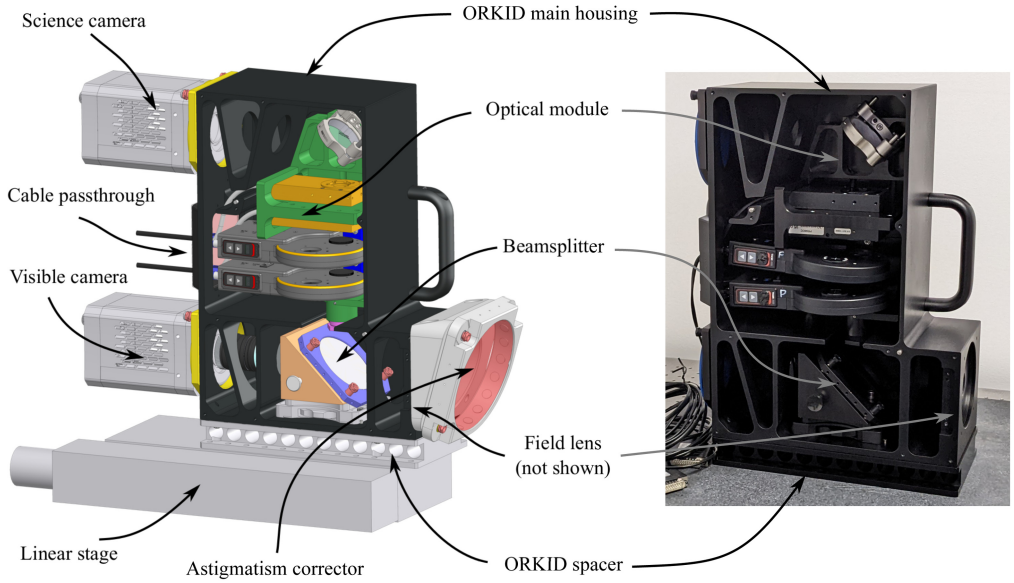

Fig. 6 Internal components of the ORKID instrument.

on a linear stage (MikroPrecision P/N NE-RS-12) previously used for the visible acquisition camera. An aluminum spacer and shims provide vertical adjustability to the instrument. The ORKID unit is positioned on the spacer via dowel pins to provide a repeatable interface and can be removed independently.

Two Andor cameras (Marana 4B-11) are mounted on an interface plate that uses three adjustment sleeves to account for the uncertainties of the position of the sensor of the cameras with regard to the mounting features. These sleeves allow adjustment in piston (±5 mm), pitch (±2 deg), and yaw (±2 deg).

The 100-mm field lens (Ross Optical P/N L-PCX391) is mounted directly at the entrance of the main housing and kept in place using an off-the-shelf threaded retaining ring (Thorlabs SM4RR). The curvature of the lens ensures self-centering when the retainer ring is installed.

The beamsplitter optic is mounted in a subcell using radial RTV (room temperature vulcanizing) adhesive dots to provide a strain-free mounting. The subcell is mounted on a 45-deg support using adjustment sleeves that provide 3 degrees of freedom to the beamsplitter (i.e., piston, pitch, and yaw). The beamsplitter support is mounted on an off-the-shelf kinematic mount (Newport M-BLK-4) to provide repeatable positioning when the beamsplitter is replaced. Two mounted beamsplitters were provided to test different coatings. Figure 7 shows the beamsplitter mounted in its subcell.

Following the beamsplitter, the optical module (shown in Fig. 8) was designed to mount the motorized components, the custom triplet, and the fold mirror. It is precisely located by dowel pins inserted in the main housing.

The triplet is mounted in a subcell that provides adjustability along the optical axis. The clear aperture of the subcell and its retaining ring were tailored to provide stray light reduction. The filter wheels (Thorlabs P/N FW102C) are mounted on interface plates that allow for their removal without requiring the removal of the instrument from the AO bench. The interface plates have dowel pins for repeatability, and captive fasteners ensure ease of assembly and disassembly. The first filter wheel (called the pupil wheel) is perpendicular to the optical path, whereas the second filter wheel (called the filter wheel) is placed at a 4-deg angle to reduce ghost reflections.

A pupil mask, shown in Fig. 9, needed to be positioned precisely in the pupil wheel. Due to the lack of reference features on the off-the-shelf filter wheel, an alignment tool was designed to use the bearings and the bore of the opposite filter mount to locate the pupil mask. Two locating pins on the alignment tool interface with a hole and a slot in the pupil mask. The alignment tool was printed with a resin printer to ensure high precision and a good fit. It should be noted that the pupil mask is placed on top of an AR-coated 3-mm-thick window (shown in green in Fig. 9) to maintain the optical path length. A retaining ring is torqued before removing the alignment tool.

Due to the shortage of the chosen baseline rotary stages because of the industrial challenges posed by the COVID-19 pandemic, the optical module was designed so that two alternative stages (i.e., Phyzik Instrumente U-651 and Newport PR50CC) could be integrated into the opto-mechanical module. The Newport stages were implemented.

Each Risley Prism is mounted in a subcell that is inserted in the rotary stage. As seen in Fig. 10, both subcells are identical in size and the prisms are held in place with an off-the-shelf

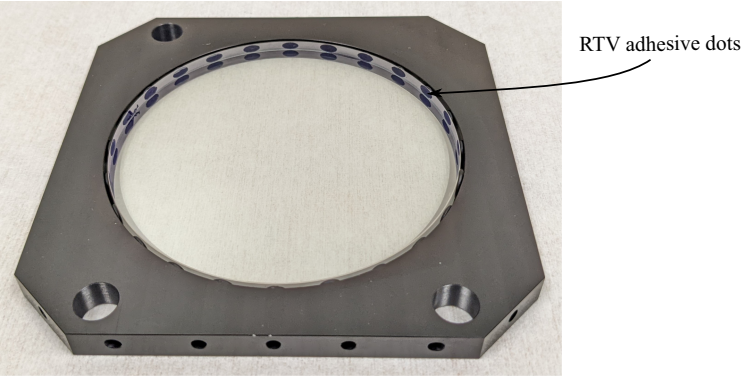

Fig. 7 Beamsplitter radially bonded in its mount using RTV adhesive dots.

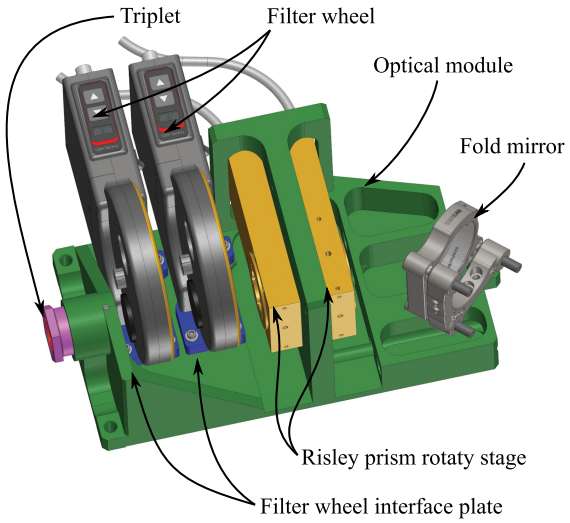

Fig. 8 Components included on the optical module.

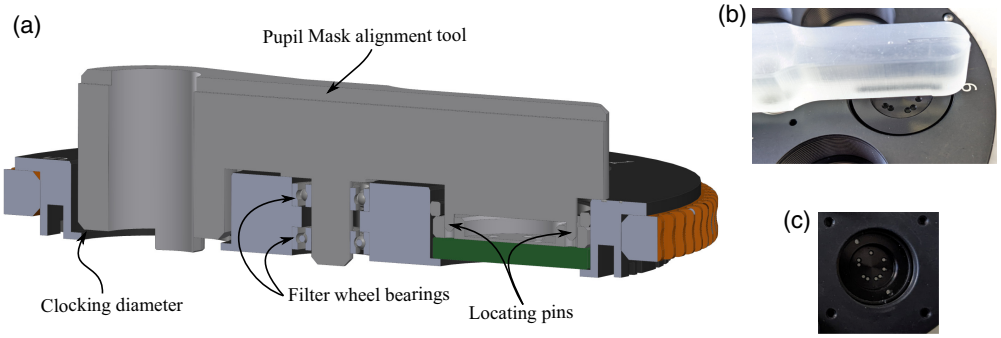

Fig. 9 Mask alignment jig. (a) Cross-section of the CAD model of the alignment tool. (b) Testing of the alignment tool. (c) Pupil mask installed.

retaining ring (Thorlabs SM20RR). The axial placement of the subcells was not critical, so they were placed using a caliper. A retaining ring included with the PR50CC rotary stage acts as a jam nut to the subcell.

The 50-mm-fold mirror (Thorlabs PF20-03-G01) is mounted in an off-the-shelf kinematic mount (Thorlabs K2) that offers 3 degrees of freedom (i.e., piston, pitch, and yaw). To reduce the stress on the mirror, it was glued radially in the mount using RTV (Dow Corning 732) and the clamping feature of the mount was not used.

The ACP was added in front of the field lens. Due to difficulties procuring the optic and the short timeline, a 3D-printed support was designed to provide the ability to modify it quickly. The printed part integrated machined adjusters and metal-threaded inserts to provide adjustability and durability. Similar to the beamsplitter, the ACP is bonded radially in its mount using RTV adhesive dots (as shown in Fig. 11).

This modular approach provides a future-proof design to implement improved optical designs with a minimum number of new opto-mechanical components.

Optical tolerances were provided at the beginning of the project to the mechanical team. These requirements were pragmatic and addressed as such by minimizing the number of parts and by the proper tolerancing of locating features inside and between modules. Not all requirements are met right at assembly, but proper adjustment mechanisms were introduced to correct potential dimensional errors. Adjustment mechanisms were being set at their nominal position for initial verification. A simple alignment procedure and related hardware were developed to ensure a quick and proper alignment if nominal positioning is not sufficient.

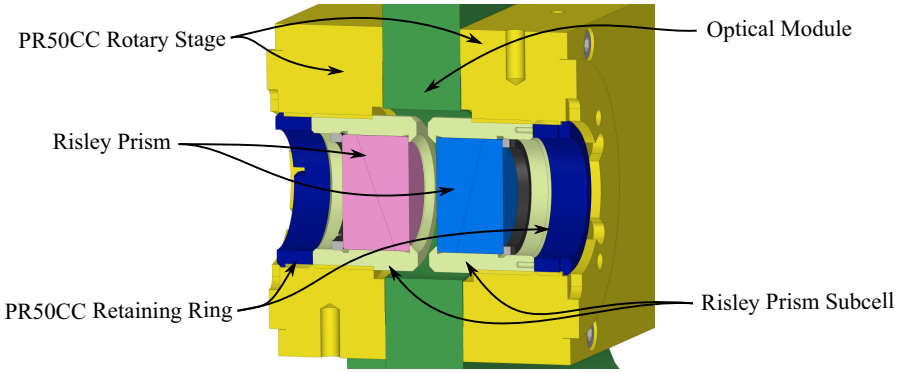

Fig. 10 Cross-section of the Risley ADC pair.

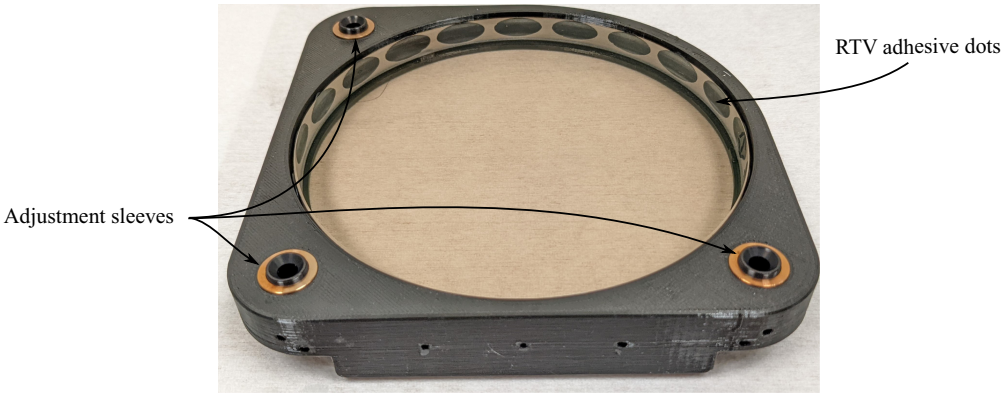

Fig. 11 ACP radially bonded in its 3D-printed mount using RTV adhesive dots.

4.3 Filters

Table 1 lists the science filters installed in the ORKID filter wheels, specifically each filter wavelength range and transmission. In addition, we plot the transmission curve for each filter in Fig. 12.

4.4 Software Systems Design

The ORKID camera server software is implemented in Python and combines the interface to the camera with a web server and a keyword server. The web server enables browser-based graphical user interface (GUIs), which can be built using readily available tools. The keyword server provides the standard interface that is common to all Keck instruments. The interface to the Andor camera is implemented through the vendor-supplied C-based library, which communicates with the camera via Universal Serial Bus (USB). A Python wrapper for this library was built using the C Foreign Function Interface (CFFI) library allowing the software to be written in Python. The main components of the camera servers are as follows:

- Andor camera interface: Interfaces to the vendor-provided library.
- HTTP web server: Provides web services for the web-based GUI.
- Data writer: Provides asynchronous writing of Flexible Image Transport System (FITS) files to disks.
- Keck Keywords interface: Retrieves telescope and AO telemetry via keywords and provides the ORKID keyword service.
- Control GUI: Web-based GUI to control and monitor the camera, as well as to display the images.

The selected camera is the Andor Marana by Oxford Instruments. Table 2 shows the frame rates for different areas of interest. The Andor Marana specification gives the maximum frame

Table 1 ORKID bandpass filters. T_{Peak} & T_{Avg} refer to the peak and average transmission values. ES_{10-90} refer to the average bandpass edge slope from 10 to 90%.

Wideband filters	λ_{Min}	λ_{Max}	λ_{Center}	T_{Peak}	T_{Avg}	ES_{10-90}
27052 R-Band Bessell	554 nm	696 nm	625 nm	—	93%	—
27058 i Sloan	698 nm	853 nm	771 nm	—	95%	—
27059 z Sloan	830 nm	1000+ nm	—	—	90%	—
Narrowband filters						
[OI]	620 nm	640 nm	630 nm	90%	—	—
H-alpha Continuum Filter	634 nm	646 nm	643 nm	90%	—	1.21 nm
27002 H-alpha	651 nm	661 nm	656.3 nm	94%	—	1.95 nm
27012 Jovian Methane	871 nm	907 nm	889 nm	—	94%	1.96 nm
CT940/20	920 nm	960 nm	940 nm	93%	—	2.57 nm

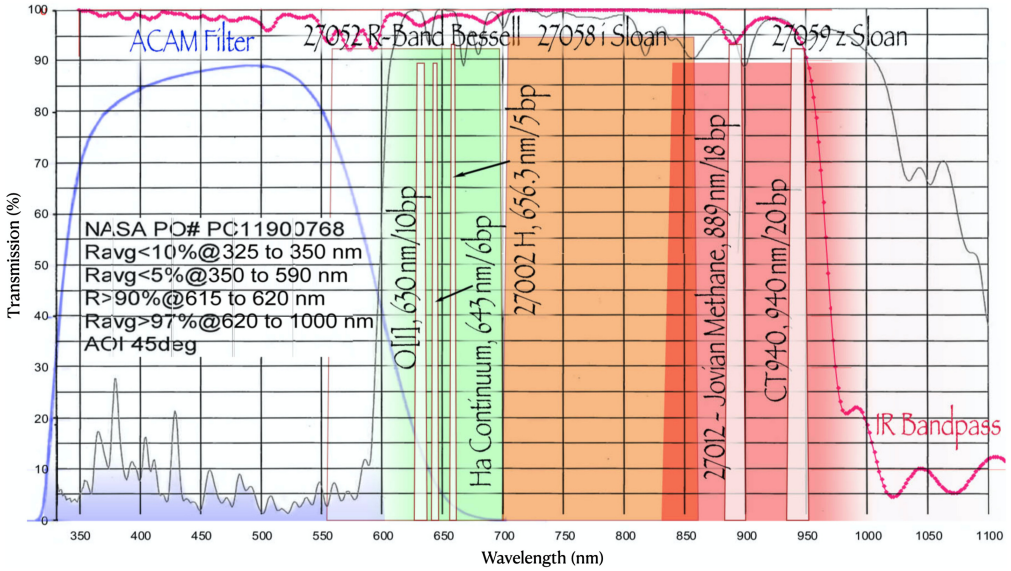

Fig. 12 Transmission curves for each filter listed in Table 1. The green-, orange-, and red-shaded areas correspond to 27052 R-Band Bessel, 27058 i Sloan, and 27059 z Sloan broadband filters, respectively. The narrowband filters reported in Table 1 are shown by the white rectangles passing in front of each shaded region, and each one is labeled.

rates. The frame rates were measured using the current implementation of the camera server for SDR (12 bits) and HDR (16 bits) read-out modes.

The camera frames are saved to disk in FITS format at the maximum transfer rate of 211 MB/s. This requires the use of fast disk storage systems. Fortunately, commercially available Solid-State Disks such as the implemented Samsung PM893 7 TB can achieve 530 MB/s write speed. To decouple the synchronous readout of the camera frames from the fluctuation of the data I/O process, a first in, first out (FIFO) data queue is used.

5 Performance Analysis

In a review of how well ORKID performs, we compare the expected value versus the actual value for the quantifiable science and technical requirements delineated in Sec. 3.1 of this report, as well as those discussed in the ORCAS Mission architecture.[2]

As can be seen from Table 3, ORKID has met the requirements listed in Sec. 3.1.

Table 2 Maximum frame rate for different areas of interest.

Area of interest (pixels)	Andor Spec max SDR rate (fps)	Measured SDR rate (fps)	Transfer SDR rate (MB/sec)	Andor Spec max HDR rate (fps)	Measured HDR rate (fps)	Transfer SDR rate (MB/sec)
32 × 32		738	2		594	1
64 × 64		594	5		427	4
128 × 128	750	427	15	378	274	9
256 × 256	378	274	36	190	159	21
512 × 512	190	159	84	95	87	46
1024 × 1024	95	87	181	30	45	95
2048 × 2048	48	45	211[a]	24	23	194

[a]Lower rate due to dropped frames.

The plate scale as well as the plate scale tolerance were calculated by moving a white light source, with the filter wheel in the open position, and observing the change in the pixel position. The same source and filter wheel configuration was also used to verify that there was no vignetting in the science field (see Fig. 13).

Figure 14 displays the simulated wavefront error, confirming that the root mean square (RMS) wavefront error across the visible camera system optics is <50 nm.

It is difficult to capture the throughput of the visible science camera using a single value, as the throughput is wavelength-dependent. As such, no single value was reported. Despite this, the throughput of the visible camera was over 90% for the wavelength range 595 to 970 nm.

Table 3 Requirements set forth in Sec. 3.1 and if they were met. The requirement numbers in the table correspond to the numbers in Sec. 3.1. For more details, see Figs. 13 and 14.

Req #	Requirement name	Expected value	Actual value	Satisfied	(D)esigned/(M)easured
1	Pixel scale	≤6.7 mas/pixel	6.65 mas/pixel	Y	M
2	Plate scale tolerance	$\leq \pm 0.1$ mas/pixel	−0.05 mas/pixel	Y	M
3	Unvignetted science field	≥10 arcsec diameter	≤3% vignetting	Y	M
4	Transmitted wavefront Quality	≤50 nm (rms)	≤50 nm (rms)	Y	D
5	Visible Camera Throughput	≥90%	≥90%	Y	D
6	2″ × 2Prime; Field Readout Time	≤10 ms	4.12 ms, 7.19 ms[a]	Y	M
7	DAR Correction	$\frac{1}{4}\lambda/D$	$\frac{1}{4}\lambda/D$	Y	M
8	DAR Over 100 nm Band	$\frac{1}{4}\lambda/D$	$\frac{1}{4}\lambda/D$	Y	M
9	Science Camera Filter Changer	≥6	8	Y	M
10	Pupil plane proximity	Close to pupil plane	Mask in pupil plane	Y	D
11	Filters	Science defined	8 science filters	Y	M
12	Unvignetted Acquistion Field	≥120″ diameter	120″ diameter	Y	D
13	Co-mounted Cameras	Co-mounted	Co-mounted	Y	M
14	Beamsplitter	Dichroic	Dichroic	Y	D

[a]The readout time is 4.12 ms when operating in SDR mode and 7.19 ms when operating in HDR mode.

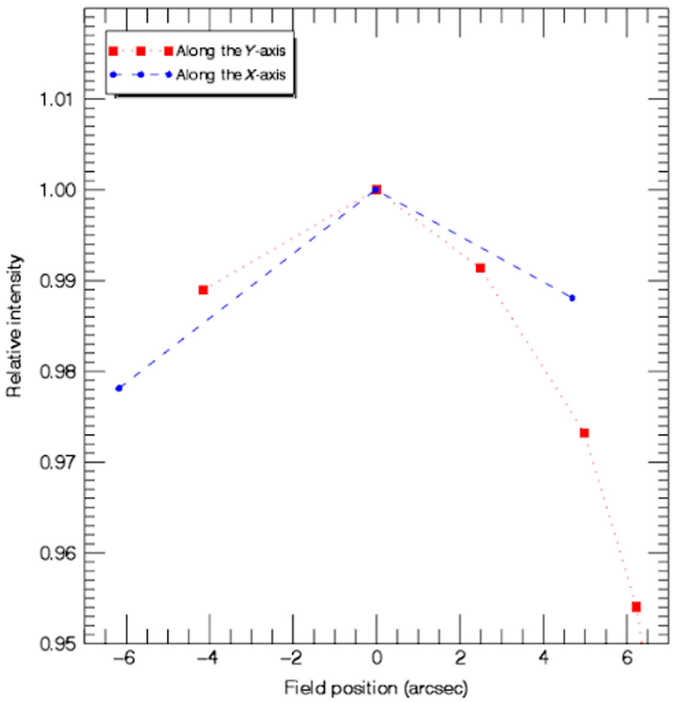

Fig. 13 Empirical test to check for vignetting. Findings demonstrate that within 5″ of off-axis distance, there is less than 3% loss in intensity satisfying the 10″ diameter unvignetted science field requirement.

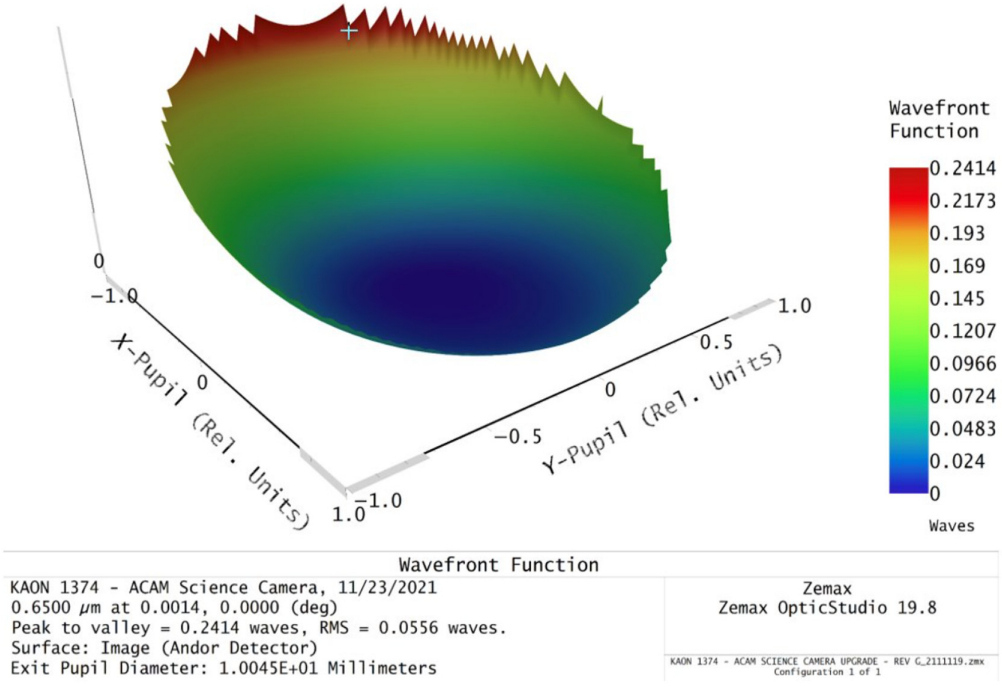

Fig. 14 Plot of wavefront error, in units of waves, across the pupil. This demonstrates that the wavefront error is <50 nm RMS across the field. The RMS wavefront error is 0.0556 waves, which, at 650 nm, equates to a 36-nm RMS wavefront error.

Although Table 2 does not explicitly list the readout time for a $2'' \times 2''$ field, the readout rate was measured to be as listed in the table.

6 On-Sky Data

ORKID was installed behind the Keck II AO System in the fall of 2022 and has been on-sky for a total of 2.5 nights of engineering time. For the first 2 nights of observing, spread across October 2022 to February 2023, ORKID was used in conjunction with the visible-light Shack-Hartmann wavefront sensor (SHWFS) and its atmospheric dispersion compensator (ADC) was not yet operational. The SHWFS can be fed either by a 96-4 beamsplitter, with 4% of the light being passed on to ORKID, or with the LGS dichroic, where all the visible light is passed to ORKID except for a 20-nm FWHM notch around the sodium 589-nm line used for LGS wavefront sensing. To pass enough light to ORKID to facilitate several ms readout times, ORKID was operated using the LGS dichroic. The reduced light going to the SHWFS resulted in a performance drop equal to making the host star roughly 2 magnitudes fainter. Here, we present a small number of observations from the Oct. 22 to Feb. 2023 timeframe, that provide a preliminary view of the instrument performance, with a more detailed characterization left for future work.

Figure 15 shows an example of ORKID data obtained with the Keck II AO system, using the SHWFS. The binary system SAO153301 was observed for 200 5-ms exposures in the CT940/20 filter on the night of January 17, 2023 UT. The system has a combined $V = 8.71$ magnitude,[42] confirmed as a multiple star system with radial velocity measurements.[43] Figure 15 shows the binary star exposures averaged with the AO loop open (no correction), the AO loop closed (high-order DM correction and tip/tilt correction), and the AO loop closed as well as a shift and add procedure applied as post-processing to the individual 5 ms exposures. The procedure recentered the exposures assuming the brightest pixel to be the center of the PSF core. Comparing the three images it is clear that the AO system provided significant gains in PSF quality, yet there was a residual tip/tilt component that needed to be corrected, leveraging the fast read-out rates.

On November 2, 2022, UT ORKID observed Θ Ori C, a known binary with a separation previously estimated to be 32.64 ± 0.48 mas using the visible-light camera of MagAO in December 2012.[44] Note that due to orbital motion this exact position is expected to change over time. Θ Ori C was observed for 40,000 10 ms exposures in the H-α filter. Individual short exposures were recentered using the brightest pixel as the central pixel, and then, all exposures were averaged for a final image. Figure 16 displays the final images created by averaging different fractions of the individual 40,000 exposures, selected based on their peak pixel value. Using the final summed image (i.e., no frame selection applied; "Selection Fraction = 1″ in the Figure), we fit a PSF model composed of four separate Gaussian profiles Astropy modeling infrastructure: two for the cores of the point sources and two to characterize the speckle halo. We find a flux ratio between the two central Gaussian components (corresponding to the two-point source cores) of ∼1.5 and a separation of ∼45 mas. The central Gaussian component, representing the PSF core, has a FWHM of ∼2.2 pixels or ∼15 mas.

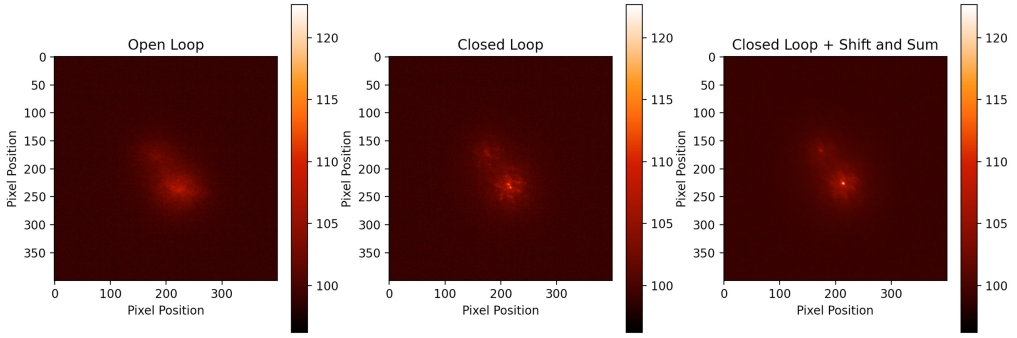

Fig. 15 ORKID images of the object SAO 153301 binary, comparing the results when the AO loop is open, versus when the AO loop is closed, versus closed loop and a recentering procedure (shifting the brightest pixel to always be aligned). To create each image 200 5-ms exposures were averaged. The color bar displays the counts/image.

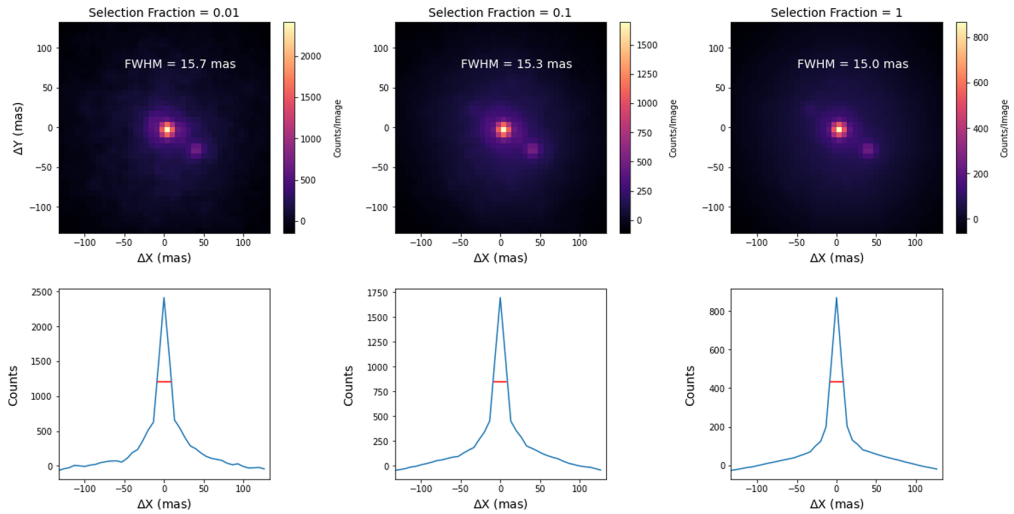

Fig. 16 Top row: Final ORKID $H-\alpha$ images of Θ Ori C, after averaging different fractions of the total image set, where the selections were made based on the highest peak pixel value in each exposure. The full dataset consisted of 40,000 10-millisecond exposures. Bottom row: Brightness profiles of the row that contains the brightest pixel in the corresponding 2D image. The red horizontal lines indicate the FWHM of the PSF core, as measured using the Gaussian profile fitting.

In addition to a Gaussian-shaped PSF, we also explored various combinations of Airy disks and Moffat profiles for the central core and for the extended AO speckle halo. We found that no specific combination provided a significant gain in the RMS residuals. We have also attempted to use a high-pass filter to spatially filter out the broad background halo. In all cases, the FWHM of the central core of the PSF was in the 14.5 to 16 mas range.

The left panel of Fig. 16 suggests that the core PSF is more complicated than just a simple Gaussian, as a hint of a first Airy ring can be seen. However, we did not find that an Airy ring provided significantly better RMS residuals than using just a Gaussian core. Indeed, the unexpected trend that the FWHM increases as fewer frames are selected could possibly be due to the fact that the fitting process is latching onto the Airy ring-like feature, artificially increasing the FWHM. As the selection fraction gets smaller, the Airy ring-like feature becomes more prominent, thus explaining the increase in FWHM. A more detailed analysis of the PSF morphology is beyond the scope of this publication but is the subject of ongoing research projects.

In Aug. 2023, the ADC was commissioned and, in addition, ORKID was operated with the NIR pyramid wavefront sensor. Analysis of this data is ongoing and will be presented in a future publication.

On September 19, 2024, ORKID performed additional observations during one-half of an engineering night. Near the end of the night, Jupiter's volcanic moon Io was observed through a variety of filters (see Table 4). We present three images of Io captured through three filters in Fig. 17. From these images, one can easily resolve the complex structure of Io's surface. We note that minimal reduction was performed on these images. A simple "shift-and-add" approach was employed to improve the signal-to-noise. Improvements in data reduction will be implemented in future work.

We also highlight observations performed on the asteroid Vesta. The asteroid has a mean diameter of roughly 530 km, which places its angular size to be $\sim 0.4''$. If we refer to ORKID's image of Vesta in Fig. 18, we find that the surface is fully resolved. Furthermore, we can use ORKID's image to estimate an angular size that is comparable ($\sim 0.3''$).

The red giant star Betelgeuse was also targeted by ORKID. The dying star serves as a fascinating target for many reasons. Perhaps the most exciting prospect is the possibility to resolve its surface with ORKID. Previous studies on Betelgeuse estimate its angular diameter to have a value between $\approx 0.04''$ and $0.06''$.[45,46] In Fig. 19, we present two images of Betelgeuse captured by ORKID through the H-Alpha and CT940/20 filters. Each image was built by simply stacking all exposures after alignment through shifting. From these images, we argue that have indeed

Table 4 Breakdown of each sky run.

Target	Filter(s)	DM loop state	Airmass	Total exposure time	Date
Θ Ori C	H – α	Closed	1.12	40,000 × 10 ms per frame	November 1, 2022
SAO 153301	CT940/20	Closed	1.25	200 × 5 ms per frame	January 17, 2023
SAO 153301	CT940/20	Open	1.25	200 × 5 ms per frame	January 17, 2023
Io	CT940/20	Closed	1.01	5 × 1000 ms per frame	September 19, 2024
Io	Hα	Closed	1.01	5 × 500 ms per frame	September 19, 2024
Io	Sloan z	Closed	1.01	5 × 100 ms per frame	September 19, 2024
Betelgeuse	H-Alpha	Closed	1.03	1000 × 1 ms per frame	November 2, 2022
Betelgeuse	CT940/20	Closed	1.03	1000 × 1 ms per frame	November 2, 2022
Vesta	CT940/20	Closed	1.76	10 × 4000 ms per frame	August 2 and 3, 2023

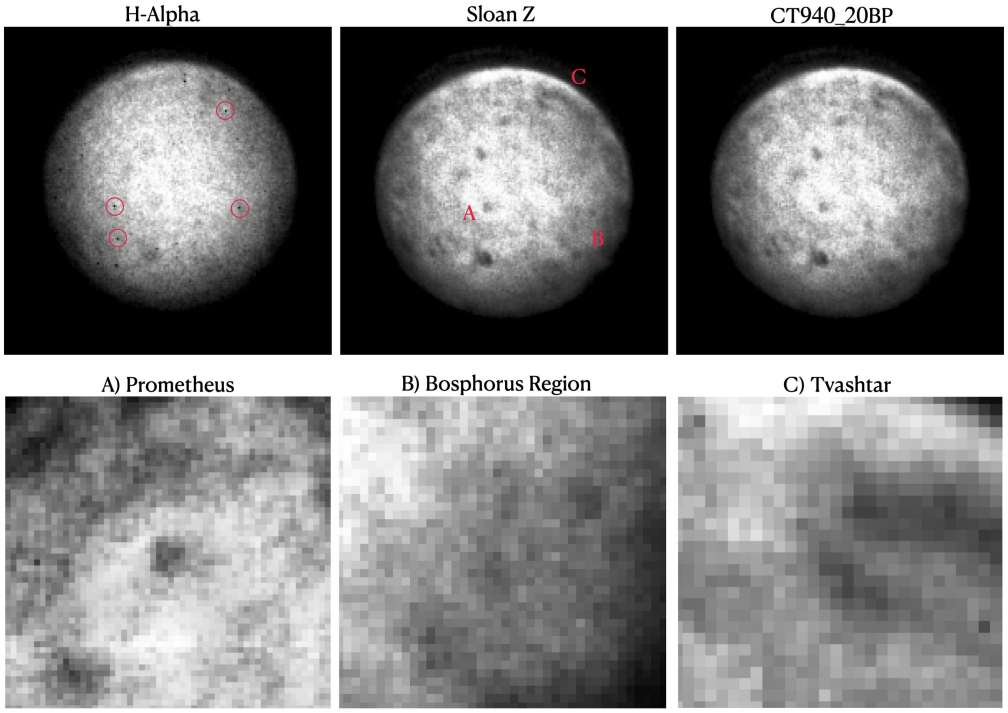

Fig. 17 Jupiter's volcanic moon Io. In the top row, we present images taken with ORKID through the H-Alpha, Sloan z, and CT940/20 filters, respectively. In addition, we zoom in on three features easily identified in the Sloan z image. Specifically, the two volcanoes Prometheus and Tvashtar, as well as the Bosphorus Region.

resolved the photosphere and measure an angular diameter of ∼0.052″, which is in agreement with previous observations.

7 Conclusion

The ORKID instrument has successfully demonstrated its ability to deliver high-resolution visible-light imaging with the Keck II AO system, achieving a FWHM of 15.2 mas at 650 nm. This accomplishment highlights the potential of large ground-based telescopes to reach near-diffraction-limited performance using advanced AO technology, enabling unprecedented

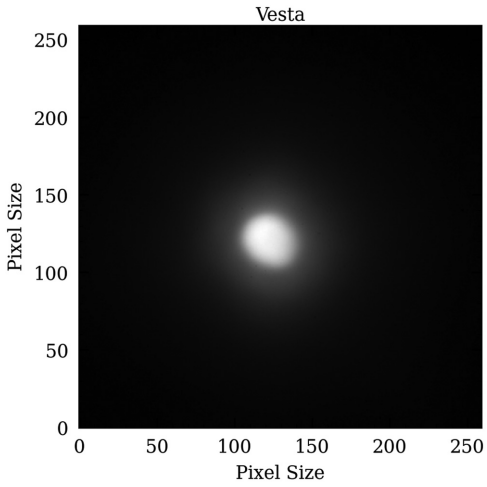

Fig. 18 Asteroid Vesta observed by ORKID through the CT940/20 filter.

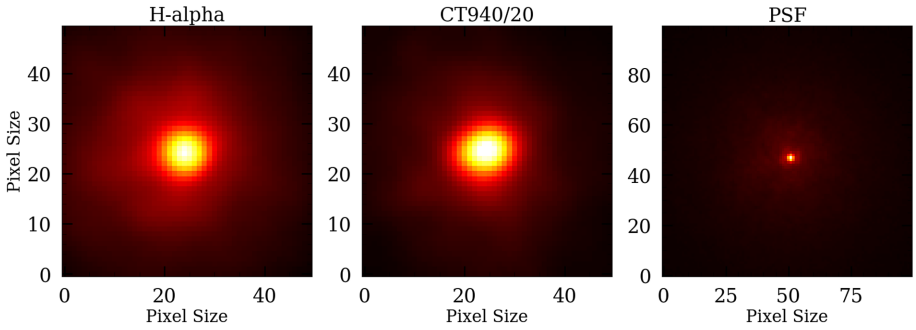

Fig. 19 Betelgeuse imaged by ORKID through two filters. From left to right, we present the H-alpha image, CT940/20, a single-star PSF image obtained immediately after observing Betelgeuse for comparison.

detail in visible-wavelength observations. The ability to resolve such fine details will significantly enhance our understanding of a wide range of astronomical phenomena in the future, from the dynamics of binary stars to the atmospheres of planets and moons in the solar system. Addressing the limitations caused by atmospheric turbulence and making visible-light AO a viable tool for future scientific endeavors.

In addition to its technical achievements, ORKID serves a critical role as a pathfinder for the larger ORCAS mission, which aims to create a hybrid ground-space observatory. Looking ahead, the continued evaluation and enhancement of ORKID's performance will be essential to further improving its capabilities. The upcoming upgrades to the Keck II AO system, including the integration of a higher actuator count deformable mirror and faster real-time control systems, promise even better performance, especially when using bright guide stars. These advancements, coupled with the insights gained from ORKID's current achievements, will guide the next steps which will include using Asteroids as guide stars and utilizing space-born lasers as additional demonstrations and TRL advancement mechanisms. This in turn will inform the final design and development of the ORCAS mission. Ultimately, ORKID's success highlights the potential for collaborative space-ground observatory systems to revolutionize visible-light astronomy, bridging the gap between current ground-based systems and future flagship space telescopes.

The key programmatic goals, identified in Sec. 2.2, were accomplished. ORKID retired ORCAS risk by demonstrating and characterizing the Keck II AO system's performance at visible wavelengths, as well as informing the future design of the ORCAS-WMKO mission instruments. The joint project also successfully fostered collaboration between the ORCAS mission and WMKO teams.

As a pathfinder instrument, the evaluation and characterization of ORKID is an ongoing process. Future goals for the project include a thorough characterization of the AO performance, more detailed instrument characterization, and consideration for facilitation upon the delivery of the high-order AO system HAKA.

Disclosures

The authors declare there are no financial interests, commercial affiliations, or other potential conflicts of interest that have influenced the objectivity of this research or the writing of this paper.

Code and Data Availability

This work made use of Astropy: (http://www.astropy.org) a community-developed core Python package and an ecosystem of tools and resources for astronomy.[47–49]

The data that support the findings of this article will be available via the Keck Observatory Archive (KOA). They can also be requested directly from the author at eliad.peretz@nasa.gov.

Acknowledgments

The WMKO is operated as a scientific partnership among the California Institute of Technology, the University of California, and the National Aeronautics and Space Administration. The Observatory was made possible by the generous financial support of the W. M. Keck Foundation. Funding for ORCAS instrument development was provided by NASA - CIF and Goddard IRAD program.

We would like to thank our industrial partners: Optimax team - Pierce Morgan, Steve Powers, Laura Capperell. Chroma Technology Corp. - Dick Stewart. OMP Inc. - Jean-Thomas Landry, Marc-André Boucher. Spectrum Thin Films - Tony Pirera, Derek Scomburg. Optical Planz Inc. - Kevin McKeon. All provided custom high-grade products at high speed which without this project would not have met its schedule and technical goals.

The authors wish to recognize and acknowledge the very significant cultural role and reverence that the summit of Mauna Kea has always had within the indigenous Hawaiian community. We are most fortunate to have the opportunity to conduct observations from this mountain.

References

1. F. Patat, O. S. Ugolnikov, and O. V. Postylyakov, "Orbiting configurable artificial star (orcas) for visible adaptive optics from the ground," *Astron. Astrophys.* **455**, 385–393 (2006).
2. E. Peretz et al., "ORCAS–orbiting configurable artificial star mission architecture," *Proc. SPIE* **11819**, 1181905 (2021).
3. E. Peretz et al., "Orbiting configurable artificial star multi-wavelength laser payload," *Proc. SPIE* **11820**, 118200F (2021).
4. E. Peretz et al., "Orbiting laser configuration and sky coverage: coherent reference for Breakthrough Starshot ground-based laser array," *J. Astron. Telesc. Instrum. Syst.* **8**(1), 017004 (2022).
5. E. Peretz et al., "Astrostationary orbits for hybrid space and ground-based observatories," *J. Astron. Telesc. Instrum. Syst.* **8**(1), 014004 (2022).
6. E. Peretz et al., "The orbiting configurable artificial star (orcas) mission," tech. rep., NASA/GSFC (2021).
7. P. Wizinowich et al., "First light adaptive optics images from the Keck II Telescope: a new era of high angular resolution imagery," *Publ. Astron. Soc. Pac.* **112**, 315 (2000).
8. P. L. Wizinowich et al., "The W. M. Keck Observatory laser guide star adaptive optics system: overview," **118**, 297–309 (2006).
9. J. M. Brase et al., "Wavefront control system for the Keck telescope," *Proc. SPIE* **3353**, 517–521 (1998).
10. B. A. Smith et al., "Voyager 2 in the Uranian system: imaging science results," *Science* **233**, 43–64 (1986).
11. B. A. Smith et al., "Voyager 2 at Neptune: imaging science results," *Science* **246**, 1422–1449 (1989).
12. I. de Pater et al., "Record-breaking storm activity on Uranus in 2014," *Icarus* **252**, 121–128 (2015).
13. L. A. de Pater et al., "High S/N Keck and Gemini AO imaging of Uranus during 2012-2014: new cloud patterns, increasing activity, and improved wind measurements," *Icarus* **258**, 192–223 (2015).
14. A. A. Simon, M. H. Wong, and A. I. Hsu, "Formation of a new great dark spot on Neptune in 2018," *Geophys. Res. Lett.* **46**, 3108–3113 (2019).
15. E. Molter et al., "Analysis of Neptune's 2017 bright equatorial storm," *Icarus* **321**, 324–345 (2019).

16. C. Cantrall et al., "Variability and geologic associations of volcanic activity on Io in 2001-2016," *Icarus* **312**, 267–294 (2018).
17. E. L. Nielsen et al., "Dynamical mass measurement of the young spectroscopic binary V343 Normae AaAb resolved with the Gemini Planet Imager," *Astron. J.* **152**, 175 (2016).
18. G. Cugno et al., "A search for accreting young companions embedded in circumstellar disks. High-contrast Hα imaging with VLT/SPHERE," *Astron. Astrophys.* **622**, A156 (2019).
19. A. Zurlo et al., "The widest Hα survey of accreting protoplanets around nearby transition disks," *Astron. Astrophys.* **633**, A119 (2020).
20. S. Sallum et al., "Accreting protoplanets in the LkCa 15 transition disk," *Nature* **527**, 342–344 (2015).
21. I. Mendigutía et al., "Spectro-astrometry of the pre-transitional star LkCa 15 does not reveal an accreting planet but extended Hα emission," *Astron. Astrophys.* **618**, L9 (2018).
22. T. Currie et al., "No clear, direct evidence for multiple protoplanets orbiting LkCa 15: LkCa 15 bcd are likely inner disk signals," *Astrophys. J. Lett.* **877**, L3 (2019).
23. S. Y. Currie et al., "Two accreting protoplanets around the young star PDS 70," *Nat. Astron.* **3**, 463–463 (2019).
24. Y. Zhou et al., "Hubble Space Telescope UV and Hα measurements of the accretion excess emission from the Young Giant Planet PDS 70 b," *Astron. J.* **161**, 244 (2021).
25. S. C. Eriksson et al., "Strong Hα emission and signs of accretion in a circumbinary planetary mass companion from MUSE," *Astron. Astrophys.* **638**, L6 (2020).
26. N. Choksi and E. Chiang, "Testing planet formation from the ultraviolet to the millimetre," *Mon. Not. R. Astron. Soc.* **510**, 1657–1670 (2022).
27. C. Z. Bond et al., "Adaptive optics with an infrared pyramid wavefront sensor at Keck," *J. Astron. Telesc. Instrum. Syst.* **6**, 039003 (2020).
28. J. Magorrian et al., "The demography of massive dark objects in galaxy centers," *Astron. J.* **115**, 2285–2305 (1998).
29. K. Gebhardt et al., "A relationship between nuclear black hole mass and galaxy velocity dispersion," *Astron. J.* **539**, L13–L16 (2000).
30. K. Gültekin et al., "The M-σ and M-L relations in galactic bulges, and determinations of their intrinsic scatter," *Astron. J.* **698**, 198–221 (2009).
31. N. J. McConnell and C.-P. Ma, "Revisiting the scaling relations of black hole masses and host galaxy properties," *Astrophys. J.* **764**, 184 (2013).
32. A. Toomre, "Mergers and some consequences," in *[Evolution of Galaxies and Stellar Populations]*, B. M. Tinsley and R. B. Gehret, Eds., p. 401 (1977).
33. J. E. Barnes and L. Hernquist, "Formation of dwarf galaxies in tidal tails," *Nature* **360**, 715–717 (1992).
34. J. Hernquist and M. J. Hernquist, "Quasars and galaxy formation," *Astron. Astrophys.* **331**, L1–L4 (1998).
35. G. Kauffmann and M. Haehnelt, "A unified model for the evolution of galaxies and quasars," *Mon. Not. R. Astron. Soc.* **311**, 576–588 (2000).
36. P. F. Hopkins et al., "Stellar feedback and bulge formation in clumpy discs," *Mon. Not. R. Astron. Soc.* **427**, 968–978 (2012).
37. C. Rodriguez et al., "A compact supermassive binary black hole system," *Astron. J.* **646**, 49–60 (2006).
38. S. Satyapal et al., "Buried AGNs in advanced mergers: mid-infrared color selection as a dual AGN candidate finder," *Astron. J.* **848**, 126 (2017).
39. R. W. Pfeifle et al., "Buried black hole growth in IR-selected mergers: new results from Chandra," *Astron. J.* **875**, 117 (2019).
40. M. Koss et al., "Host galaxy properties of the swift bat ultra hard X-ray selected active galactic nucleus," *Astron. J.* **739**, 57 (2011).
41. M. J. Koss et al., "A population of luminous accreting black holes with hidden mergers," *Nature* **563**, 214–216 (2018).
42. N. Zacharias et al., "VizieR online data catalog: UCAC4 catalogue (Zacharias+, 2012)," VizieR Online Data Catalog, I/322A (2012).
43. G. A. Zacharias, "Pulkovo compilation of radial velocities for 35 495 Hipparcos stars in a common system," *Astron. Lett.* **32**, 759–771 (2006).
44. L. M. Close et al., "Diffraction-limited visible light images of orion trapezium cluster with the magellan adaptive secondary adaptive optics system (MagAO)," *Astron. J.* **774**, 94 (2013).
45. I. Close et al., "The angular diameter of Betelgeuse," *Astron. Astrophys.* **115**, 253–256 (1982).
46. J. Weiner et al., "Precision measurements of the diameters of α orionis and o ceti at 11 microns," *Astrophys. J.* **544**, 1097 (2000).

47. T. P. Robitaille et al., "Astropy: a community Python package for astronomy," *Astron. Astrophys.* **558**, A33 (2013).
48. A. M. Price-Whelan et al., "The Astropy Project: building an open-science project and status of the v2.0 core package," *Astrophys. J.* **156**, 123 (2018).
49. A. M. Price-Whelan et al., "The Astropy Project: sustaining and growing a community-oriented open-source project and the latest major release (v5.0) of the core package," *Astrophys. J.* **935**, 167 (2022).

Biographies of the authors are not available.